ARTICLE OPEN

Check for updates

Microenvironmental Snail1-induced immunosuppression promotes melanoma growth

Marta Arumi-Planas[1], Francisco Javier Rodriguez-Baena[1], Francisco Cabello-Torres[1], Francisco Gracia[1], Cristina Lopez-Blau[1], M. Angela Nieto[1,2] and Berta Sanchez-Laorden[1]✉

Melanoma is an aggressive form of skin cancer due to its high metastatic abilities and resistance to therapies. Melanoma cells reside in a heterogeneous tumour microenvironment that acts as a crucial regulator of its progression. Snail1 is an epithelial-to-mesenchymal transition transcription factor expressed during development and reactivated in pathological situations including fibrosis and cancer. In this work, we show that Snail1 is activated in the melanoma microenvironment, particularly in fibroblasts. Analysis of mouse models that allow stromal Snail1 depletion and therapeutic Snail1 blockade indicate that targeting Snail1 in the tumour microenvironment decreases melanoma growth and lung metastatic burden, extending mice survival. Transcriptomic analysis of melanoma-associated fibroblasts and analysis of the tumours indicate that stromal Snail1 induces melanoma growth by promoting an immunosuppressive microenvironment and a decrease in anti-tumour immunity. This study unveils a novel role of Snail1 in melanoma biology and supports its potential as a therapeutic target.

Oncogene (2023) 42:2659–2672; https://doi.org/10.1038/s41388-023-02793-5

Graphical Abstract

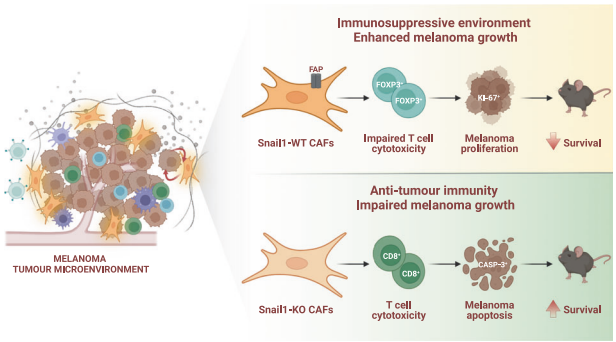

INTRODUCTION

Melanoma is the most aggressive form of skin cancer. If found early, it can be surgically resected, but melanoma is extremely metastatic and very resistant to treatments when disseminated to other organs. Even though in recent years the landscape of melanoma treatment has greatly improved with the use of more effective targeted therapies and immunotherapies, not all patients respond to these treatments and many of the patients who respond develop resistance after a relatively short period of disease control [1]. Importantly, melanoma progression and how it responds to treatments is strongly influenced by the tumour microenvironment (TME) [2].

Epithelial to mesenchymal transition (EMT) is a developmental process that can be triggered in pathological conditions including fibrosis and cancer. Epithelial cells undergo EMT acquiring the capacity to move and disseminate [3, 4]. EMT endows cancer cells with invasive and migratory capabilities as the tumour progresses [5, 6]. The main inducers of the EMT are transcription factors (TFs) of the Snail, Twist and Zeb families. EMT-TFs coordinate the downregulation of epithelial genes and the induction of mesenchymal ones [3, 7]. EMT-TFs play an important role in the development and dissemination of epithelial-derived carcinomas, particularly when they are expressed in tumour cells [3, 8, 9] but also when their expression is associated with stromal cells, particularly cancer-associated fibroblasts (CAFs) [10–14]. CAFs, central components of the tumour stroma, are a complex and heterogeneous population of myofibroblasts whose activity associates with tumour aggressiveness. CAFs coordinate a wide array of functions including matrix remodelling, angiogenesis, and tumour-promoting immune evasion [15, 16].

[1]Instituto de Neurociencias (CSIC-UMH), Sant Joan d'Alacant, Spain. [2]CIBERER, Centro de Investigación Biomédica en Red de Enfermedades Raras, ISCIII, Madrid, Spain. ✉email: berta.lopez@umh.es

Received: 7 February 2023 Revised: 13 July 2023 Accepted: 19 July 2023
Published online: 29 July 2023

Reprogramming in the expression of different EMT-TFs, including Zeb1/2, Twist and Snail2 in melanoma cells is associated with tumour progression [17–21]. In addition, previous studies have assessed the impact of Snail1-induced EMT in melanoma cells [22–24]. However, whether Snail1 expression in the TME regulates melanoma biology has not been investigated. In this study, we use different mouse models to unveil a novel immunoregulatory role of Snail1 reactivation in the melanoma microenvironment. We show that Snail1 expression in fibroblasts regulates fibroblast activation protein alpha (Fap) expression and promotes immunosuppression. Consistent with the latter, Snail1 targeting significantly decreases tumour and metastatic burden, increasing mice survival. We also show that the effects driven by microenvironmental Snail1 targeting are associated with an increase in anti-tumour immune responses. Altogether, this indicates that stromal Snail1 has a crucial role in shaping the melanoma microenvironment to drive tumour progression.

RESULTS

Snail1 reactivation in the tumour microenvironment promotes melanoma growth

Snail1 expression has been previously found in epithelial and stromal cells in carcinomas [11, 25]. To characterise the expression of Snail1 in melanoma, and to distinguish tumour cells from the cells in the TME, we generated a melanoma reporter mouse model by crossing the inducible BRAF-driven mouse melanoma model $Braf^{CA}$,$Pten^{loxP}$,Tyr::CreERT2 ($Braf^{V600E}$/$Pten^{loxP}$) [26] with Rosa-LSL-tdTomato mice (tdTomato). Tamoxifen treatment of these mice results in melanoma development with a short latency [26] and the expression of the Tomato fluorescent protein in melanocytes and melanoma cells. Analysis of this model showed SNAI1 expression restricted to tdTomato-negative cells in the tumours (Fig. 1a, b) indicating that *Snail1* is reactivated in the melanoma microenvironment but not in the melanoma cells. To specifically target the stroma, we next generated a syngeneic melanoma model by injecting murine $Braf^{V600E}$-5555 cells [27, 28] in UBC-Cre-ERT2 mice [29] crossed with tdTomato mice (Fig. 1c). In this model, tamoxifen treatment promotes the ubiquitous expression of the Tomato fluorescent protein in the mouse, allowing to trace the red labelled stromal cells in the allografts. Analysis of the tumours confirmed SNAI1 expression in the recombined cells from the melanoma microenvironment that was absent in normal skin (Fig. 1d). We extended our analyses to additional oncogenic BRAF and $BRAF^{wt}$/$NRAS^{wt}$ melanoma syngeneic models and confirmed SNAI1 reactivation in the stroma of these tumours (Supplementary Fig. 1). Next, we wanted to assess the contribution of microenvironmental Snail1 ($Snail^{ME}$) to melanoma growth. For this, UBC-Cre-ERT2-tdTomato mice were bred with $Snai1^{fl/fl}$ mice [30] to prevent Snail1 reactivation in the tumour stroma. Melanomas were established by subcutaneous injection of $Braf^{V600E}$-5555 cells in UBC-Cre-ERT2-tdTomato and UBC-Cre-ERT2-tdTomato-$Snai1^{fl/fl}$ (referred as $Snail1^{ME}$-WT and $Snail1^{ME}$-KO, respectively) (Fig. 1c). When the tumours were already established, animals were treated with tamoxifen to block stromal Snail1 expression and melanoma growth was monitored (Fig. 1e). We confirmed that recombined stromal cells from $Snail1^{ME}$-KO mice lack SNAI1 expression (Fig. 1f). Importantly, melanoma growth was blocked and significantly reduced in $Snail1^{ME}$-KO compared to $Snail1^{ME}$-WT mice (Fig. 1g, h). In line with these results, we observed a decrease in the proliferation of melanoma cells from $Snail1^{ME}$-KO tumours (Fig.1i, j) and a significant increase in apoptotic melanoma cells as indicated by cleaved-Caspase 3 (Fig. 1k, l). These results show that Snail1 is expressed in the melanoma microenvironment where it is necessary for melanoma growth.

Snail1 reactivation in melanoma-associated fibroblasts decreases anti-tumour immunity

Expression of Snail1 and other EMT-TFs have been reported in macrophages and CAFs from epithelial-derived tumours [10–14]. To investigate Snail1 expression in these cell populations in melanoma, we first analysed $Braf^{V600E}$-5555 tumours grown subcutaneously in Cx3cr1CreERT2-YFP reporter mice. These mice constitutively express YFP in the myeloid lineage including monocytes and macrophages [31, 32]. We did not detect SNAI1 on myeloid cells in our tumours (Fig. 2a) or in additional immune populations as assessed by CD45 staining (Fig. 2b, Supplementary Fig. 2a). On the contrary, we detected SNAI1 expression in melanoma-associated fibroblasts, as indicated by double tdTomato-PDGFRα positive staining (Fig. 2c). SNAI1 positive expression in melanoma-associated fibroblasts was further confirmed in the melanoma transgenic $BRAF^{V600E}$/$Pten^{loxP}$/tdTomato model (Fig. 2c). We also validated SNAI1 expression in $PDGFR\alpha^{+}$ cells by using PDGFRα-CreERT2-tdTomato reporter mice (Supplementary Fig. 2b) and confirmed that blocking SNAI1 expression in $PDGFR\alpha^{+}$ fibroblasts reduced melanoma growth (Supplementary Fig. 2c).

To determine the mechanisms implicated in Snail1 contribution to melanoma growth, we isolated $tdTomato^{+}PDGFR\alpha^{+}$ cells from $Braf^{V600E}$-5555 tumours grown in $Snail1^{ME}$-WT and $Snail1^{ME}$-KO mice after tamoxifen treatment and performed RNA sequencing (Fig. 2d, Supplementary Fig. 3a). We corroborated that isolated cells were positive for PDGFRα, SNAI1, and αSMA, an additional CAF marker (Supplementary Fig. 3b), and confirmed *Snai1* downregulation in $tdTomato^{+}PDGFR\alpha^{+}$ cells from $Snail1^{ME}$-KO mice (Supplementary Fig. 3c). Among the 520 differentially expressed genes (DEGs) detected upon Snail1 targeting, 323 were upregulated and 197 downregulated (Fig. 2e). In agreement with the role of Snail1 in embryonic development, gene ontology (GO) analysis of the upregulated genes showed an enrichment in biological processes associated with morphogenesis and differentiation (Fig. 2f) [33, 34]. On the contrary, 11 out of the 15 most enriched biological processes in the downregulated genes were associated with the immune system (Fig. 2f). In addition, gene set enrichment analysis (GSEA) [35] showed that melanoma-associated fibroblasts were enriched in signatures related to TGFβ signalling and fibroblast activation in carcinomas and this correlation was decreased upon Snail1 targeting (Fig. 2g). We also found that several of the downregulated genes including *Ccl1*, *Ccl22*, *Cxcl13* or *Ccr7* were associated with immunosuppression and decreased anti-tumour immunity [36–40] (Supplementary Fig. 3d, e). Additional GO and GSEA analyses confirmed a significant decrease in processes and genes associated with immunosuppression and pro-inflammatory pathways in Snail1 depleted melanoma-associated fibroblasts [41] (Fig. 2g, h, Supplementary Fig. 3f). Interestingly, comparison of our transcriptomic data with melanoma stromal scRNAseq data [42] showed that $tdTomato^{+}PDGFR\alpha^{+}$ cells from $Snail1^{ME}$-WT tumours were enriched in the signatures related to the S1 ("immune") and S2 ("desmoplastic") CAFs subpopulations (Fig. 2i). Critically, the most significant difference between $tdTomato^{+}PDGFR\alpha^{+}$ cells from $Snail1^{ME}$-WT and $Snail1^{ME}$-KO tumours corresponds to the signature of the S1 ("immune") population, associated to higher expression of immunomodulatory factors [42]. Further, we also compared our transcriptomic data with an additional dataset from breast cancer CAFs defined as immunosuppressive [43] and confirmed that $tdTomato^{+}PDGFR\alpha^{+}$ cells from $Snail1^{ME}$-WT were enriched in the signature associated to immunosuppression and, this correlation was decreased upon Snail1 targeting (Fig. 2j).

Altogether, our data suggest that the anti-tumour effects observed upon Snail1 targeting in the melanoma microenvironment may be related to CAFs immunoregulatory functions. To test this hypothesis, we characterised the immune infiltration in $Braf^{V600E}$-5555 melanomas upon $Snail1^{ME}$ depletion (Fig. 3a). We observed that compatible with the impaired growth of

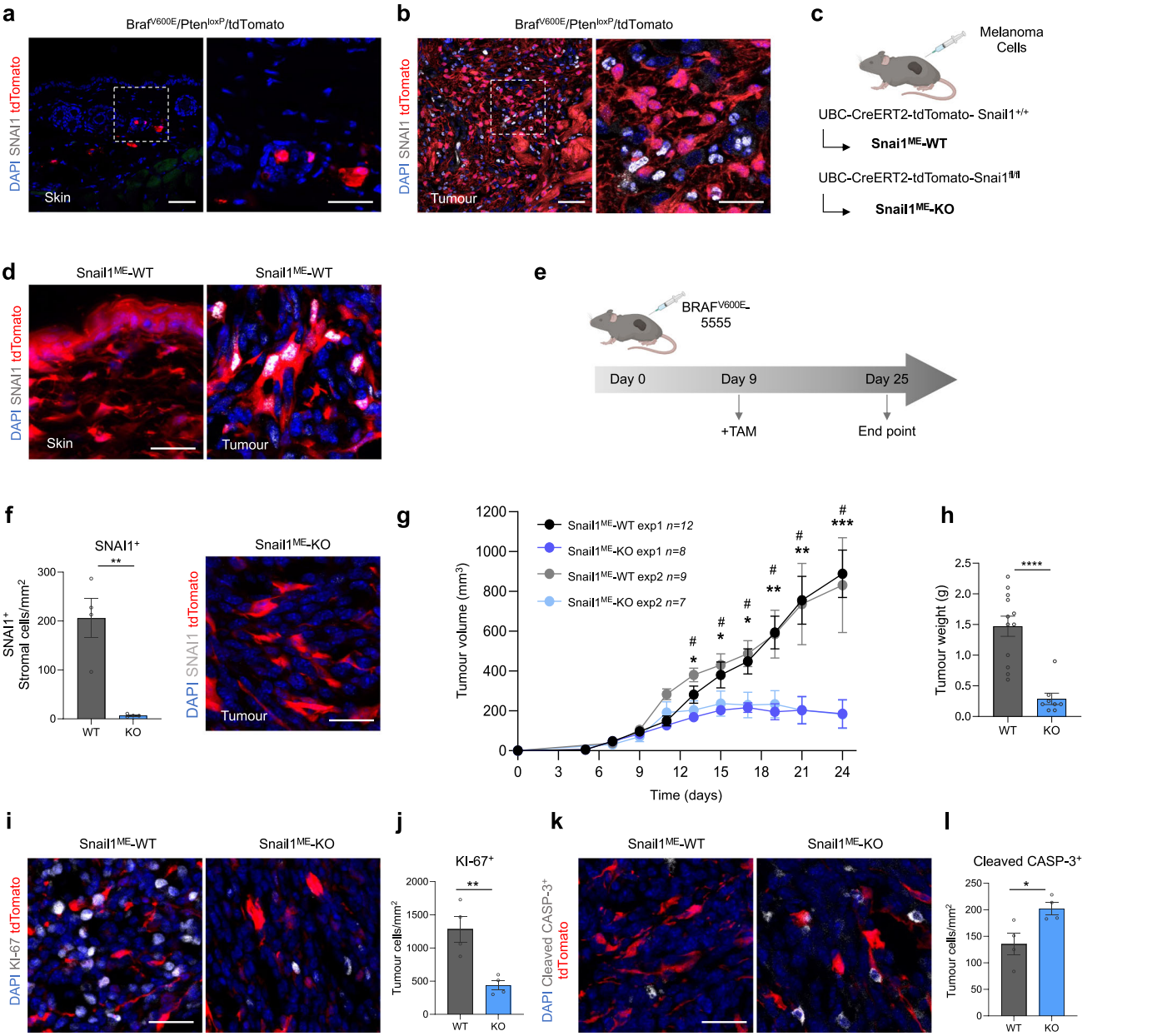

Fig. 1 Snail1 is expressed in the melanoma microenvironment and its ablation reduces tumour growth and promotes apoptosis. **a**, **b** Representative images of immunolabelling for SNAI1 (white) in control skin and tumours from Braf^{CA}, Pten^{loxP}, tdTomato, Tyr::CreERT2 (Braf^{V600E}/Pten^{loxP}/tdTomato) mice. Melanoma cells are labelled in red (tdTomato). **c** Mouse models generated to investigate the impact of Snail1 on the melanoma microenvironment. **d** Representative images of immunolabelling for SNAI1 (white) in control skin (left panel) and Braf^{V600E}-5555 tumours (right panel) from Snail1^{ME}-WT mice. Stromal cells are labelled in red (tdTomato). **e** Experimental set-up of the in vivo strategy design to study the contribution of Snail1 to melanoma progression. Created with BioRender.com. **f** Quantification of SNAI1^{+} stromal cells ($n = 4$ per condition) (left panel) and representative image of immunolabelling for SNAI1 (white) in Snail1^{ME}-KO tumours upon tamoxifen administration (right panel). Stromal cells are labelled in red (tdTomato). **g** Braf^{V600E}-5555 tumour growth was assessed in two independent experiments combined in this graph (exp1 $n = 12$ Snail1^{ME}-WT and $n = 8$ Snail1^{ME}-KO; exp2 $n = 9$ Snail1^{ME}-WT and $n = 7$ Snail1^{ME}-KO). **h** Final weight after collection of tumours from Snail1^{ME}-WT (WT) and Snail1^{ME}-KO (KO) mice ($n = 12$ WT; $n = 8$ KO). **i** Representative images of immunolabelling for KI-67(white) in tumours from Snail1^{ME}-WT and Snail1^{ME}-KO mice. Stromal cells are labelled in red (tdTomato). **j** Quantification of KI-67 (white) tumour nuclei-positive cells in images from (**i**) ($n = 4$). **k** Representative images of immunolabelling for Cleaved-CASP3 (white) in tumours from Snail1^{ME}-WT and Snail1^{ME}-KO mice. Stromal cells are labelled in red (tdTomato). **l** Quantification of images from (**k**) ($n = 4$). Data are represented by Mean ± SEM and statistically significant differences are tested by unpaired two-tailed Student *t*-test. Each dot represents one animal (* = $p < 0.05$, ** = $p < 0.01$, *** $p < 0.001$, **** $p < 0.0001$ and # = $p < 0.05$ for experiment 2). WT = Snail1^{ME}-WT and KO = Snail1^{ME}-KO. Scale bars: 50 µm and 25 µm for higher magnification pictures.

melanomas, the percentage of tumour infiltrating cytotoxic T cells (CD8^{+}) was elevated in tumours from Snail1^{ME}-KO compared to Snail1^{ME}-WT mice (Fig. 3b). In addition, significantly fewer regulatory T cells (FOXP3^{+}) were found in Snail1^{ME}-KO tumours (Fig. 3c). Further analyses show an increase in B cells and Natural killer (NK) cells in tumours from Snail1^{ME}-KO mice, while the number of dendritic cells and myeloid cells remained constant (Fig. 3d, e). However, we detected upregulated expression of

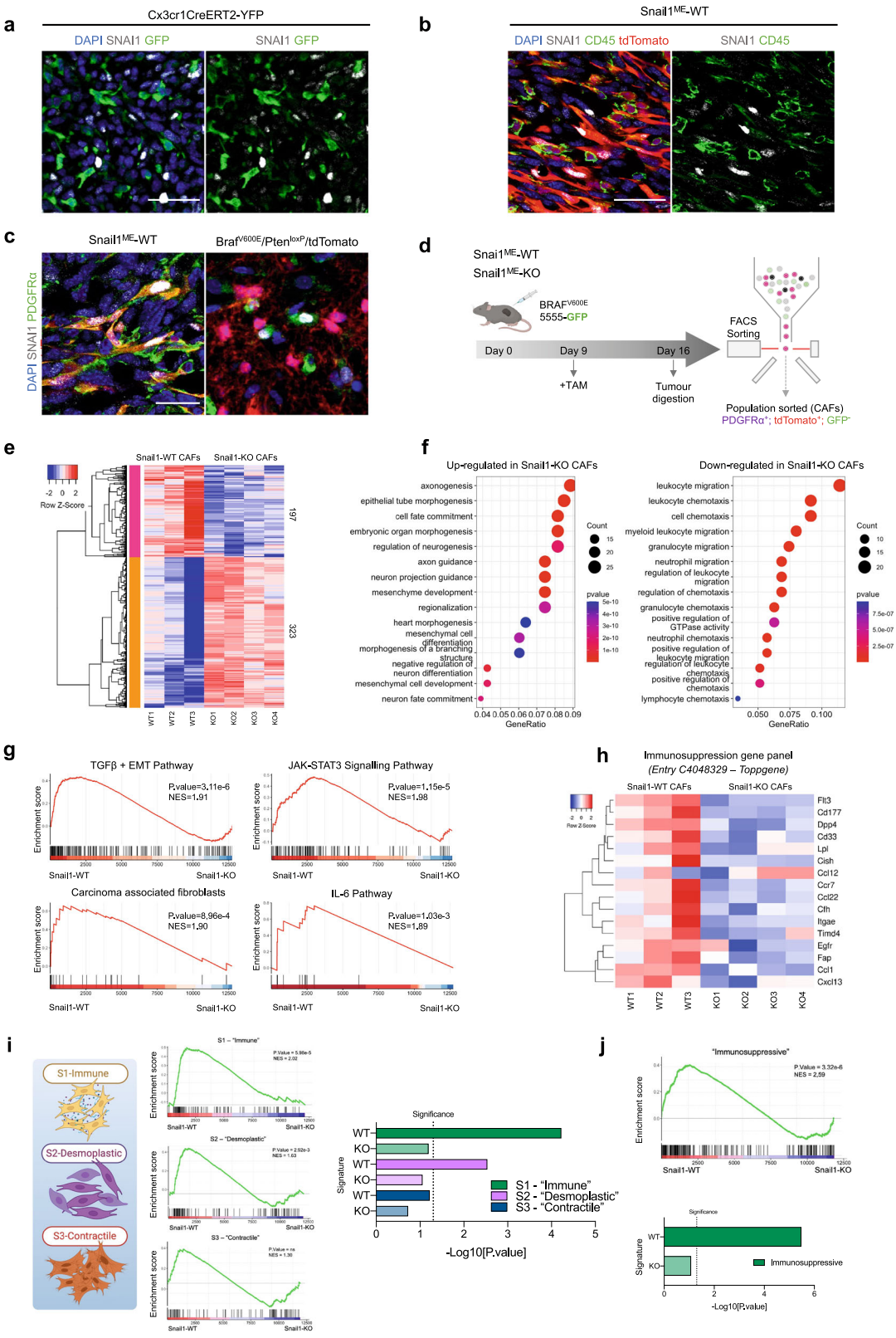

Arginase 1 (*Arg1*) (Fig. 3f) a marker associated with M2-like macrophages with immunosuppressive and pro-tumourigenic functions, in melanomas from Snail1^{ME}-WT compared to Snail1^{ME}-KO mice. Altogether, these data indicate that Snail1^{ME} expression blocks anti-tumour immune responses.

Interestingly, given our results indicating that Snail1 promotes immunosuppression in our models, and the association of immunosuppression with resistance to immunotherapy [44], we sought to investigate the correlation of Snail1 levels with clinical outcomes in patients treated with immune-checkpoint inhibitors.

Fig. 2 Snail1 expression in PDGFRα$^+$-CAFs is associated with fibroblast activation and immunosuppression signatures. a Representative images of immunolabelling for SNAI1 (white) and myeloid cells (green) in a section of a Braf^{V600E}-5555 melanoma grown in Cxcr1CreERT2-YFP mice. **b** Representative images of immunolabelling for SNAI1 (white) and CD45 (green) in melanomas from Snail1^{ME}-WT mice. Stromal cells are labelled in red (tdTomato). **c** Representative images of immunolabelling for SNAI1 (white) and PDGFRα (green) in Braf^{V600E}-5555 tumours from Snail1^{ME}-WT mice. Stromal cells are labelled in red (tdTomato) (left panel) and in BRAF^{V600E}/Pten^{loxP}/tdTomato melanomas where melanoma cells are labelled in red (tdTomato) (right panel). Scale bar: 25 µm. **d** Schematic illustration of the strategy followed to isolate fibroblasts from Braf^{V600E}-5555 melanomas in Snail1^{ME}-WT and Snail1^{ME}-KO mice. Created with BioRender.com. **e** RNAseq heatmap of differentially expressed genes (DEGs). The scale bar corresponds to row Z score in a -2–2 relationship. Filtered and normalised count per million data from the DEGs has been plotted to compare Snail1-WT and Snail1-KO CAFs. Columns represent the different samples. Each sample is a pool of three different animals with the same genotype WT $n = 3$, KO $n = 4$. **f** Representation of gene ontology enrichment analysis of the 15 top GO terms as ranked by various gene set testing methods. The dot plot size and colour represent the relative number and relevance of the genes in the set, respectively. **g** Gene set enrichment analysis (GSEA) of DEGs genes (log2 ratio-ranked) shows enrichment of TGFβ + EMT, JAK-STAT3 and IL-6 pathway signatures and enrichment of Carcinoma-associated fibroblasts signature in Snail1-WT CAFs. NES (normalised enrichment score) and p-value scores are shown. **h** Panel showing expression of genes associated with immunosuppression from entry C4048329 in the Toppgene and DisGeNet databases. **i** GSEA analysis of custom gene sets generated from DEGs in the S1 "immune", S2 "desmoplastic" and S3 "contractile" CAFs populations defined in [42]. NES (normalised enrichment score) and *p* value scores are shown, ns, not significant. Created with BioRender.com. **j** GSEA analysis of marker gene sets in the immunosuppressive breast CAF population defined in [43]. NES (normalised enrichment score) and *p* value scores are shown.

Analysis from transcriptomic datasets [45] using Kaplan-Meier Plotter [46] revealed that high Snail1 expression before or on-treatment with anti-programmed death-1 (anti-PD-1) correlated with a lower overall survival in melanoma patients (Fig. 3g, h).

Snail1 induces Fap expression in fibroblasts

Recent studies using syngeneic carcinoma models indicate that CAFs expressing FAP are responsible for immune-evasion associated with a pro-tumourigenic TME [43, 47–51]. Given our results showing that Snail1^{ME} in melanoma promotes immunosuppression and that its silencing blocks tumour growth, we next investigated the potential relationship between Snail1 and Fap in fibroblasts. First, we characterised our models. Analysis of our RNAseq data showed a decrease in *Fap* expression in melanoma-associated fibroblast upon Snail1 depletion (Supplementary Fig. 3d, e). Further, we confirmed lower levels of *Fap* mRNA in tumours from Snail1^{ME}-KO when compared to Snail1^{ME}-WT mice (Fig. 4a) and in tdTomato$^+$PDGFRα$^+$ isolated fibroblasts from those tumours (Fig. 4b). In line with this, *Fap* was downregulated in NIH3T3 fibroblasts after silencing *Snai1* expression with a siRNA (Fig. 4c) and upregulated upon TGFβ treatment or *Snai1* overexpression (Fig. 4d, e). Further, we found that CYD19, an inducer of Snail1 degradation [52], reduced *Fap* expression in NIH3T3 fibroblasts (Fig. 4f) indicating that Snail1 could be regulating *Fap* expression. We also analysed TCGA (The Cancer Genome Atlas) data from different cancers and found a positive correlation between *Snai1* and *Fap* expression in 28 tumour types including melanoma (Supplementary Fig. 4). To assess whether SNAI1 could directly bind to regulatory regions of the *Fap* promoter, we next performed chromatin immunoprecipitation (ChIP) assay in *Snail1*-overexpressing NIH3T3 cells. For this, we looked for consensus Snail1 E-boxes [53] (CANNTG) within the mouse *Fap* promoter using the SnapGene® software. Both murine and human FAP promoters contain multiple Snail1 E-boxes near their transcription start site. We considered regions with 2 or more E-boxes as predicted SNAI1 binding sites (BS), and we found several within the mouse *Fap* promoter (BS1, BS2, BS3, BS4 and BS5) (Fig. 4g). Chromatin immunoprecipitation analysis confirmed that BS1, BS2 and BS3 were highly enriched in SNAI1 binding as compared with IgG control in the NIH3T3 cell line (Fig. 4h). All this together indicates that SNAI1 could directly regulate *Fap* transcription in fibroblasts.

Snail1^{ME} targeting reduces metastatic burden and increases mice survival

Our results show that targeting Snail1^{ME} blocks subcutaneous melanoma growth. We next wanted to address whether Snail1 regulates the metastatic niche microenvironment. For this, we injected luciferase-expressing Braf^{V600E}-5555 melanoma cells in the tail vein of Snail1^{ME}-WT and Snail1^{ME}-KO mice. We confirmed that SNAI1 expression was absent in control lungs and was reactivated in the metastatic microenvironment in Snail1^{ME}-WT mice (Fig. 5a) and blocked in metastases from Snail1^{ME}-KO mice (Fig. 5a, b). We also observed SNAI1 reactivation in PDGFRα$^+$-CAFs from melanoma lung metastases in Snail1^{ME}-WT mice that was confirmed in Braf^{V600E}/Pten^{loxP}/tdTomato melanomas (Fig. 5c, Supplementary Fig. 5). When metastases were detected by bioluminescence in an IVIS in vivo imaging system, animals were treated with tamoxifen and metastases growth was monitored (Fig. 5d, e). Histological analysis of the lungs (Fig. 5f) showed a significant decrease in metastatic burden (−82.9%), metastases number (−47.6%) and size (−77.5%) in Snail1^{ME}-KO compared to Snail1^{ME}-WT mice (Fig. 5g). Further, we also investigated whether blocking Snail1^{ME} activation could improve mice survival. Kaplan-Meier analysis showed an almost 30% increase in the survival of Snail1^{ME}-KO mice, compared to Snail1^{ME}-WT, assessed by long-rank test ($X^2 = 6.92$, $p < 0.01$) (Fig. 5h). Importantly, as in the subcutaneous tumours, these anti-tumour immune effects were associated with a decrease in proliferation and an increase in apoptosis in the melanoma cells in Snail1^{ME}-KO metastases (Fig. 5i, j). We then analysed the immune infiltrate in the lungs and confirmed that metastases from Snail1^{ME}-KO mice had an increased number of cytotoxic T cells (CD8$^+$) and a lower infiltration of regulatory T cells (FOXP3$^+$) compared to Snail1^{ME}-WT metastases (Fig. 5k). Gene expression analysis also showed a decrease in *Fap* mRNA levels in lung metastases from the Snail1^{ME}-KO mice (Fig. 5l).

The data described above indicate that genetic blockade of Snail1 activation in the TME decreases metastases growth and in line with our previous results, this is associated with a less immunosuppressive environment. We had previously shown that Snail1 targeting by injection of antisense oligonucleotides could constitute a good therapeutic strategy in renal fibrosis [54]. To investigate whether this was also the case in melanoma, we used a similar approach and injected a VIVO-morpholino (VI-MO) that targets a splicing site in the *Snai1* mRNA (Snail1-MO) [54] into the tail vein of C57BL/6 mice with established Braf^{V600E}-5555 lung metastases (Fig. 6a). Once lung metastases were detected by bioluminescence, the mice were treated with VI-MOs and the signal was monitored by IVIS (Fig. 6b). Histological analysis of the lungs (Fig. 6c) showed a decrease in the weight (−56.7%), metastatic burden (−55.9%) and number of metastases (−37.4%) in the Snail1-MO as compared to Control-MO treated mice (Fig. 6d). We confirmed the efficacy of the morpholino in blocking *Snail1* expression in the lung metastases (Fig. 6e, f) that was accompanied by a decrease in *Fap* levels (Fig. 6f). Further, metastases from mice treated with Snail1-MO had increased *Cd8a* compared to Control-MO treated mice (Fig. 6g). Thus, as observed in our Snail1^{ME}-KO mice, Snail1 systemic inhibition was associated with an anti-tumour immune response and decreased melanoma metastatic burden.

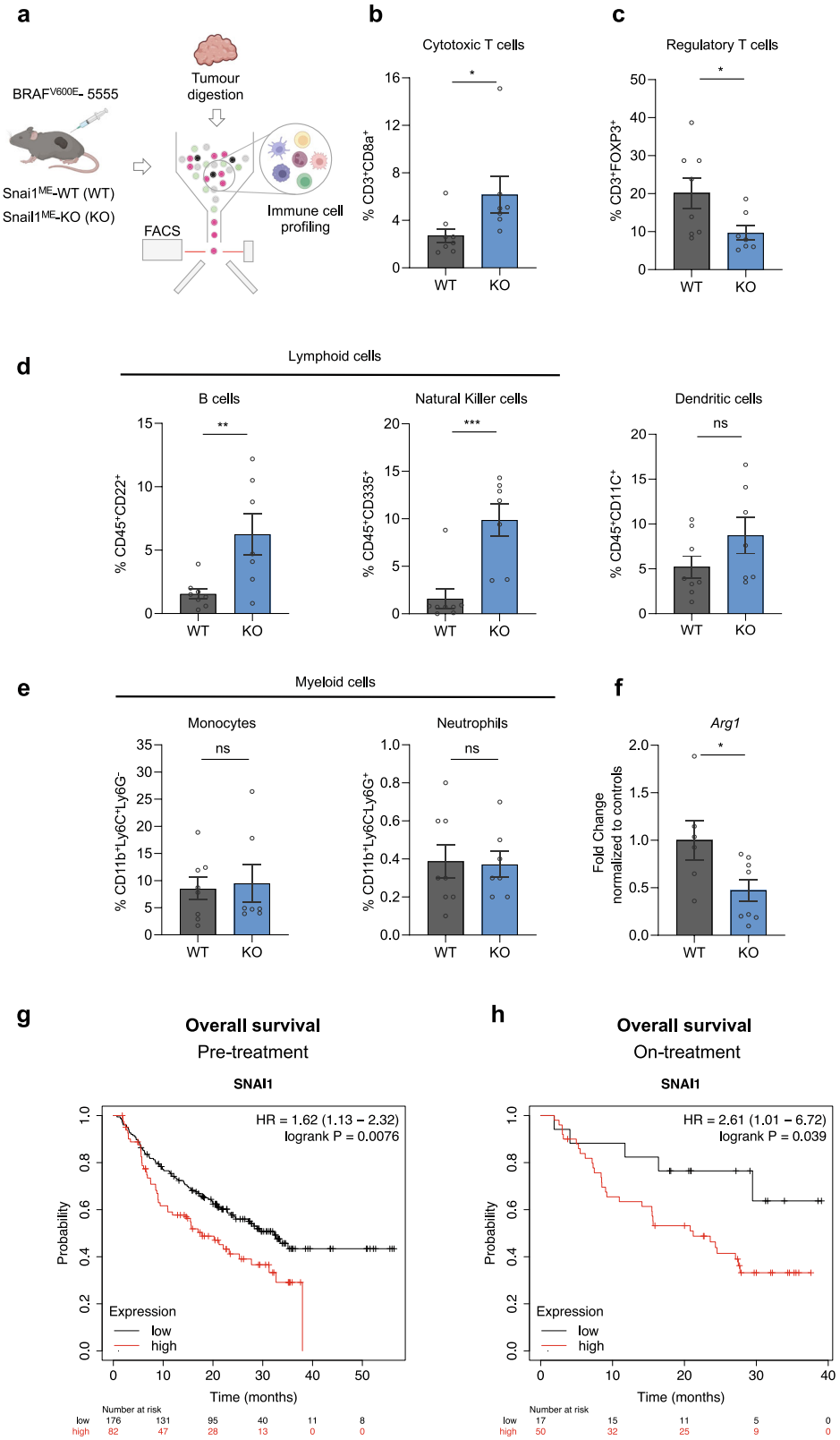

DISCUSSION

Modulation of the immune response in the TME plays a major role in the clinical response to treatments [55]. In this study, we have identified stromal Snail1 as a driver of melanoma growth by promoting an immunosuppressive TME. Moreover, Snail1 targeting is enough to reduce melanoma metastatic burden and increase mice survival.

Snail1 is an essential TF during embryonic development whereas it is mostly absent in healthy adult tissues. Snail1 reactivation is involved in fibrosis and in the progression of several

Fig. 3 Snail1^{ME} targeting induces an anti-tumourigenic immune response in melanoma. a Schematic representation of the strategy used to perform immune cell profiling by flow cytometry analysis of Braf^{V600E}-5555 melanomas in Snail1^{ME}-WT (WT) and Snail1^{ME}-KO (KO) mice. Created with BioRender.com. **b**, **c** Graphs showing percentages of Cytotoxic T cells (CD3$^+$CD8a$^+$) and Regulatory T cells (CD3$^+$FOXP3$^+$) in tumours from (a) ($n = 8$ WT and $n = 7$ KO). **d** Graphs showing percentages of lymphoid cells from (**a**); B cells (CD45$^+$CD22$^+$), natural killer cells (CD45$^+$CD335$^+$), and dendritic cells (CD45$^+$CD11c$^+$). **e** Graphs showing percentages of myeloid cells in tumours from (**a**); monocytes (CD11b$^+$Ly6C$^+$Ly6G$^-$) and neutrophils (CD11b$^+$Ly6C$^-$Ly6G$^+$), are represented ($n = 8$ WT and $n = 7$ KO). **f** *Arg1* mRNA levels detected by RT-qPCR in tumour samples from (**a**) ($n = 5$ WT and $n = 8$ KO). Data are represented by Mean ± SEM and statistically significant differences are tested by unpaired two-tailed Student *t*-test. Each dot represents one animal (ns = not significant, *=$p < 0.05$, **=$p < 0.01$, ***$p < 0.001$). **g**, **h** Prognostic value of Snail1 expression in response to anti-PD-1 therapy. Survival curves plotted for melanoma patients. *SNAI1* expression assessed before anti-PD-1 therapy ($n = 258$) or on treatment ($n = 67$). Data was analysed using Kaplan-Meier Plotter. Patients with *SNAI1* expression above the median are indicated in red line, and patients with expressions below the median in black line. HR hazard ratio.

cancer types [56], as a potent driver of the EMT process in carcinoma cells [9]. Previous studies indicated that Snail1 induction in melanoma cells promotes invasion and metastasis [22], however, Snail1 contribution to melanoma biology in an in vivo context was not defined. Our analyses of an inducible BRAF-driven melanoma reporter model reveal that SNAI1 in melanoma is reactivated in the stroma, particularly in CAFs. This is confirmed in syngeneic melanoma models where we find SNAI1 expression in CAFs in subcutaneous tumours and in lung metastases. In this study, we have generated mouse models that allow Snail1 ablation in an otherwise undisturbed immunocompetent environment to unveil the contribution of microenvironmental Snail1 to melanoma. We demonstrate that stromal Snail1 depletion blocks melanoma growth. This is associated with diminished proliferation and increased apoptosis of melanoma cells, pointing towards a non-cell autonomous role of microenvironmental Snail1 in melanoma cells. In accordance with this, Snail1 expression in CAFs from breast or colorectal cancer promotes epithelial cell invasion by paracrine signalling mediated by prostaglandinE2 [11]. Here we show that Snail1-expressing CAFs mediate a tumour-promoting phenotype in melanoma by exerting an immunoregulatory role in the tumours.

Recently, single-cell sequencing technologies have shed light into the complexity and heterogeneity of CAFs in different tumour types and a better understanding of their functions and features can be harnessed to design better therapies for cancer treatments [16, 43, 57]. Although CAFs subsets in pancreas and breast have been characterised in detail [16], less is known about CAFs modulation of melanoma biology. Recently, three different melanoma CAFs populations have been described [42] and *Pdgfra* expression was widely found in the populations enriched at early stages of melanoma progression when our CAFs transcriptomic analysis was performed. Interestingly, we find that *Fap* is highly expressed in Snail1-expressing CAFs and downregulated upon its depletion. Further, we demonstrate that SNAI1 directly binds to the *Fap* promoter indicating that Snail1 can induce FAP expression in fibroblasts. Snail1 has classically been considered a potent transcriptional repressor [25], however it can also act as a transcriptional activator [58, 59]. In carcinoma cells, Snail1 directly activates the transcription of cytokines implicated in the recruitment of tumour-associated macrophages promoting TME remodelling [58]. Moreover, we previously showed that in renal fibrosis, Snail1 reactivation in tubular epithelial cells promotes a profibrotic inflammatory microenvironment by sustaining TGFβ signalling and cytokines production [54]. We show in this study that Snail1 depletion in CAFs also impinges on pathways associated to TGFβ signalling and inflammation and into the recruitment and activation of immune cells, indicating that Snail1 has a major immunoregulatory role when expressed in the melanoma microenvironment. Further, it is known that FAP-expressing CAFs populations are associated with immunosuppressive characteristics [43, 49, 50], and that elevated FAP expression in CAFs through the JAK-STAT3 signalling pathway, contributes to a pro-tumourigenic immune response [47]. Consistently, our RNA sequencing data shows downregulation of the JAK-STAT3 signalling pathway among other pro-tumourigenic pathways when Snail1 is blocked. All these results are in line with the decrease in *Fap* levels we find in Snail1 KO-CAFs in association with anti-tumour immunity as shown by increased infiltration of cytotoxic CD8$^+$-T, B cells and NK cells, and consistent with impaired melanoma growth. FAP$^+$CAFs have also been associated with the recruitment of regulatory FOXP3$^+$-T lymphocytes [50], and in agreement with this, we find that the decrease in regulatory T cells we observe in the TME of tumours from Snail1^{ME}-KO mice favours an anti-tumourigenic phenotype.

Interestingly, the effects of blocking Snail1 reactivation in the melanoma microenvironment are not restricted to the subcutaneous compartment but extend to the metastatic niche. Microenvironmental Snail1 depletion impairs the progression of experimental lung metastases associated with decreased *Fap* levels and anti-tumour immune responses. This suggests that despite CAFs heterogeneity, Snail1 is expressed in this population in an organ-independent manner to promote immunosuppression and tumour growth. We also demonstrate that in vivo systemic targeting with a Snail1 morpholino reduces metastatic burden in mice, extending mice survival. Moreover, as Snail1 was previously associated with increased metastases by favouring immune evasion by an EMT-dependent mechanism in melanoma cells [22], our data further support Snail1 potential as a good therapeutic target in melanoma. Snail1 has been classically considered undruggable, however CYD19, a recently developed inhibitor of Snail1 protein-protein interactions, has proved efficient in impairing tumour growth in mouse models of breast cancer [52]. We show here that this compound not only blocks Snail1 expression but also decreases Fap levels in fibroblasts and considering that Snail1 expression is almost absent in healthy tissues [56], its inhibition in melanoma patients should be safe and lack major adverse effects.

The use of immune checkpoint inhibitors that target regulatory pathways on T cells to elicit anti-tumour responses has greatly improved the management of melanoma patients. However, only ~50% of patients respond [60]. Interestingly, Snail1-induced EMT in melanoma cells promoted resistance to immunotherapy based on intratumour injection of dendritic cells [22] and we show here that SNAI1 expression correlates with worse clinical responses to anti-PD-1 in melanoma patients. Current efforts directed to improve immune checkpoints inhibitors efficacy and the clinical management of patients include the characterisation of mechanisms regulating immunosuppression [44] and the discovery of biomarkers to predict responses. In this study, we show that Snail1 is a driver of CAFs-induced immunosuppression and pro-tumour immunity in melanoma, that its expression correlates with impaired responses to immune checkpoint inhibitors and therefore, we confirm its potential as a therapeutic target.

METHODS

Mice

All experiments involving animals were performed in accordance with the European Community Council Directive (2010/63/EU) and Spanish legislation. The protocols were approved by the CSIC Ethics Committee and the Animal Welfare Committee at the Instituto de Neurociencias CSIC-UMH. Mice were hosted in a pathogen-free facility under controlled temperature,

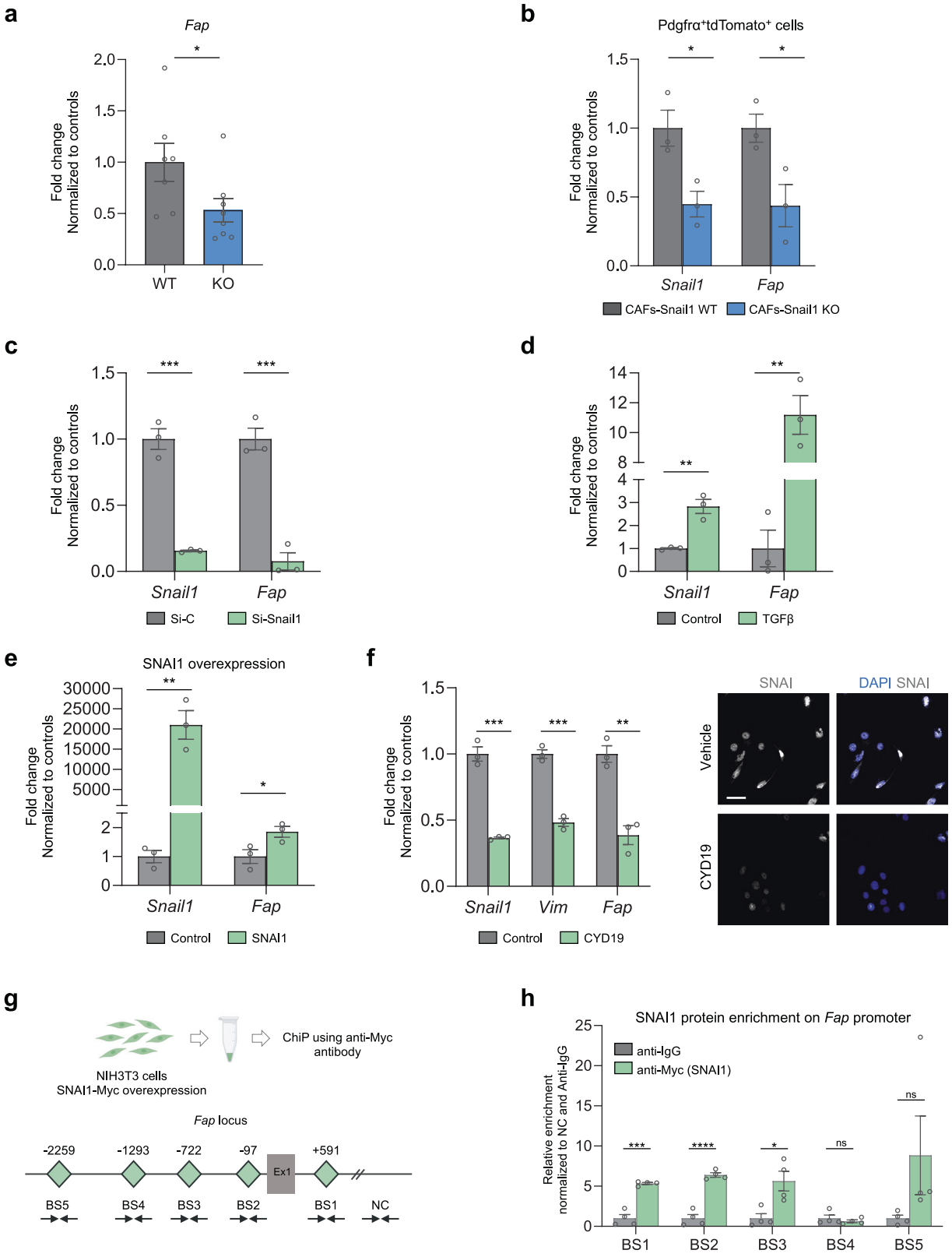

humidity, and 12 h light/dark cycle. All experiments were performed in 7–8-week-old mice C57BL/6. To analyse Snail1 in melanomas we crossed the inducible BRAF-driven mouse melanoma model $Braf^{CA}$,$Pten^{loxP}$,Tyr::-CreERT2 ($BRAF^{V600E}$/$Pten^{loxP}$) [26] (RRID:IMSR_JAX:013590) with Rosa-LSL-tdTomato (RRID:IMSR_JAX:007909) mice (referred as $Braf^{V600E}$/$Pten^{loxP}$/tdTomato). To investigate Snail1 in the TME we crossed UBC-Cre-ERT2 mice [29] (RRID:IMSR_JAX:008085) or PDGFRα-CreERT2 mice [61] with Rosa-LSL-tdTomato (tdTomato) (RRID:IMSR_JAX:007909) and $Snai1^{fl/fl}$ mice [30]. To analyse myeloid populations in tumours, we used Cx3cr1CreERT2-YFP mice (RRID: IMSR_JAX:021160).

Fig. 4 Fap is a direct target of Snail1 in fibroblasts. a *Fap* mRNA levels detected by RT-qPCR in $Braf^{V600E}$-5555 tumours from $Snail1^{ME}$-WT (WT) and $Snail1^{ME}$-KO (KO) mice ($n = 7$ WT and $n = 8$ KO). **b** *Fap* mRNA levels detected by RT-qPCR in Snail1-WT and Snail1-KO PDGFRα^{+}/tdTomato^{+} isolated fibroblasts ($n = 3$ WT and $n = 3$ KO) (**c**) *Snail1* and *Fap* mRNA levels detected by RT-qPCR upon Snail1 silencing using a siRNA in TGFβ treated NIH3T3 cells. Transfected cells were collected 48 h after transfection ($n = 3$). **d** *Snail1* and *Fap* mRNA levels increase detected by RT-qPCR upon TGFβ treatment in NIH3T3 cells. Cells were collected 48 h after TGFβ treatment ($n = 3$). **e** *Snail1* and *Fap* mRNA levels increase detected by RT-qPCR after SNAI1 transfection in NIH3T3 cells ($n = 3$). **f** *Snail1*, *Vimentin* and *Fap* mRNA levels detected by RT-qPCR in NIH3T3 cells treated with TGFβ (2 ng/ml) for 24 h and then with vehicle or CYD19 (5 nM) in the presence of TGFβ for another 48 h (left panel). Representative IF of SNAI in cells from (**f**), scale bar: 50 µm (right panel). **g** SNAI1 enrichment on the *Fap* promoter shown by ChiP assay in NIH3T3 cells, using an anti-Myc antibody (for SNAI1-Myc overexpression). Schematic representation of the mouse *Fap* locus is shown. SNAI1 potential binding sites (E-boxes; CANNTG) on the *Fap* promoter are represented as green diamonds (BS1: +591 bp, BS2: −97bp, BS3: −722bp, BS4: −1293bp, BS5 −2259bp). An intergenic region without SNAI1 binding sites was used as a negative control (NC). Ex1: SNAI1 exon 1. **h** Relative enrichment of SNAI1 binding to the five potential sites, normalised to the NC region and the anti-IgG controls ($n = 4$). Data are represented by Mean ± SEM and statistically significant differences are tested by unpaired two-tailed Student *t*-test. Each dot represents one animal (**a**) or independent experiments (**c**–**f**) (ns = not significant, * = $p < 0.05$, ** = $p < 0.01$, ***$p < 0.001$, ****$p < 0.0001$).

Cell culture

Murine melanoma cell line $Braf^{V600E}$-5555 [27, 28] was originally obtained from Richard Marais laboratory and luciferase-expressing $Braf^{V600E}$-5555 cells (5555-Luc) were kindly given by Imanol Arozarena´s lab (NavarraBiomed). $BRAF^{WT}NRAS^{WT}$-B16F10 (CRL-6475) and $BRAF^{V600E}$-YUMM1.7 (CRL-3362) cells were obtained from ATCC, and the FCT1 cell line was isolated from a tumour arising in $Braf^{V600E}/Pten^{loxP}$/tdTomato transgenic mouse in our laboratory. NIH3T3 fibroblasts (CRL1658) were purchased from ATCC. All cell lines were maintained in DMEM (Sigma) supplemented with 10% FBS (Sigma) and 1% penicillin/streptomycin (Sigma). Cells were kept at 37 °C in a humid atmosphere containing 5% CO_2 and the media was replaced every 2/3 days. Melanoma cells were passaged when they reached 80% confluency 1:10 every 72 h, while NIH3T3 cells were passaged when they reached 60–70% confluency 1:20 every 72 h. Cells were discarded up to seven consecutive passages and replaced by fresh stocks. All cell lines were tested and confirmed negative for mycoplasma monthly at the host institution.

Inducible melanoma reporter model

Tumours were induced topically in 6–8 weeks $Braf^{V600E}/Pten^{loxP}$/tdTomato mice. Treatment with 1.5 µl 4 hydroxy tamoxifen (4-HT) (Sigma) (8 mg/ml), dissolved in ethanol:DMSO (80:20), was applied on the shaved skin of the back. Mice were immobilised until 4-HT dried completely. Tumours were collected when reaching approximately 1200 mm^3 (formula: length × width × depth × 0.562).

Melanoma subcutaneous allografts

5555 melanoma cells (5×10^6 in 100ul in sterile PBS $Ca^{2+}Mg^{2}$-free) were subcutaneously injected in the dorsal area of $Snail1^{ME}$-WT and $Snail1^{ME}$-KO or PDGFRα-CreERT2/tdTomato and PDGFRα-CreERT2/tdTomato $Snail1^{fl/fl}$ 7–8 weeks old mice. Treatment with tamoxifen (Sigma) (intraperitoneally, 100 mg/kg body weight), dissolved in corn oil:ethanol (90:10), was carried out to induce recombination. Tamoxifen administration began once tumours reached a volume of 80–100 mm^3. Tumour volume was recorded with a calliper every 2/3 days. When the tumours reached the limit size the mice were sacrificed, and tumours were collected for histological analysis.

For CAFs isolation by FACS $Snail1^{ME}$-WT and $Snail1^{ME}$-KO mice were injected with GFP-expressing 5555 cells as previously described. Four doses of tamoxifen were injected intraperitoneally on alternate days before collection and processing of the tumours. To study the myeloid populations in melanoma tumours, $Braf^{V600E}$-5555 melanoma cells were injected as described previously in Cx3cr1CreERT2-YFP mice.

Experimental metastasis assay

To evaluate metastatic progression in vivo, $Braf^{V600E}$-5555 -Luc (1×10^4 cells in 100 µl of sterile PBS $Ca^{2+}Mg^{2}$-free) were intravenously injected into the lateral tail vein, using a 27-gauge needle. Lung colonisation was analysed in vivo and ex vivo by BLI. Anaesthetised mice (isoflurane) were injected intraperitoneally with D-luciferin (Perkin Elmer) (150 mg/kg body weight) and imaged with an IVIS Lumina XR imaging system (PerkinElmer). The lung BLI of every mouse was determined using Living Image software (PerkinElmer). Tamoxifen treatment (intraperitoneally, 100 mg/kg body weight) was started once experimental metastases were established and detected by BLI imaging. Tamoxifen was administered three days a week until the end of the experiment. Mice were sacrificed after 3 weeks, and tissues were collected for histological analysis.

Tumour processing

Tumours and lungs were fixed in 4% PFA for 4 h or ON respectively at 4 °C. After fixation, tumours and lungs were washed three times with PBS and incubated in 30% sucrose for three days at 4 °C before embedding in OCT. Embedded samples were kept in dry ice and transferred to −80 °C before sectioning. Finally, OCT-embedded lungs and tumours were sectioned in a cryostat (Leica) at 8 µm-thick sections and dried for 2 h at room temperature (RT) before being used for immunolabelling or stored at −80 °C.

Immunofluorescence (IF) stainings

Sections were blocked in 5% NGS, 1% BSA and 0.2% Triton x-100 for 1 h at RT and incubated with the primary antibodies O/N at 4 °C in blocking solution and the following day for 30 min at RT. After extensive washing in PBS, slices were incubated with the secondary antibodies and DAPI in a blocking solution for 1 h at RT. After washing the secondary antibody with PBS, slices were mounted in Dako Fluorescence Mounting Medium (Dako). Information and dilution of antibodies are listed in Supplementary Table 1. For IF in fibroblasts, FAC isolated cells were cultured and treated on poly-lysine (Sigma) glass coverslips in 12-well plates and fixed with 4% PFA for 15 min at RT. Afterwards, cells were washed three times with PBS, permeabilized with 0.1% Triton x-100 in PBS for 15 min and blocked in a 0.1% Triton x-100 1% BSA solution for 1 h at RT. Then, cells were incubated with the primary antibodies O/N at 4 °C in 1% BSA solution and the following day for 30 min at RT. After washing three times with PBS, cells were incubated with the secondary antibodies and DAPI 1 h at RT in 1% BSA solution. After washing the secondary antibody with PBS, cells were imaged.

Immunostainings were conducted using the primary and secondary antibodies listed in Supplementary Table 1. Pictures were taken with an Olympus FV1200 confocal microscope with 20× or 40× objectives.

Quantification of Ki-67 and cleaved Caspase-3

Proliferation and apoptosis were evaluated after IF staining by imaging sections and processing them with the ImageJ software. To analyse tumour proliferation and apoptosis, cell counts were obtained in three random fields from the tumour invasive front, three random fields from the tumour centre and three random fields from the tumour edge in each tumour slice. The same number of pictures were performed in every tumour slice. Four different tumours were analysed per condition. To analyse experimental lung metastases proliferation and apoptosis, representative pictures of different metastases were taken from each lung slice. Four different lungs were analysed per condition. The number of proliferating and apoptotic cells was determined as number of apoptotic or proliferating tumours cells/mm^2.

Histological analysis of melanoma lung metastases

8 µm-thick lung sections were prepared and stained with Haematoxylin and Eosin (H&E) (Sigma) and documented with a Leica DFC700T digital camera. To quantify lung metastatic burden, 9 serial H&E stained lung sections were collected every 150 µm, spanning a total of 1200 microns of lung tissue. Total metastatic area (metastasis area/total lung area *100), number of metastases (number of metastases/lung) and average metastasis size (total metastatic area/number of metastases) were measured using Image J software.

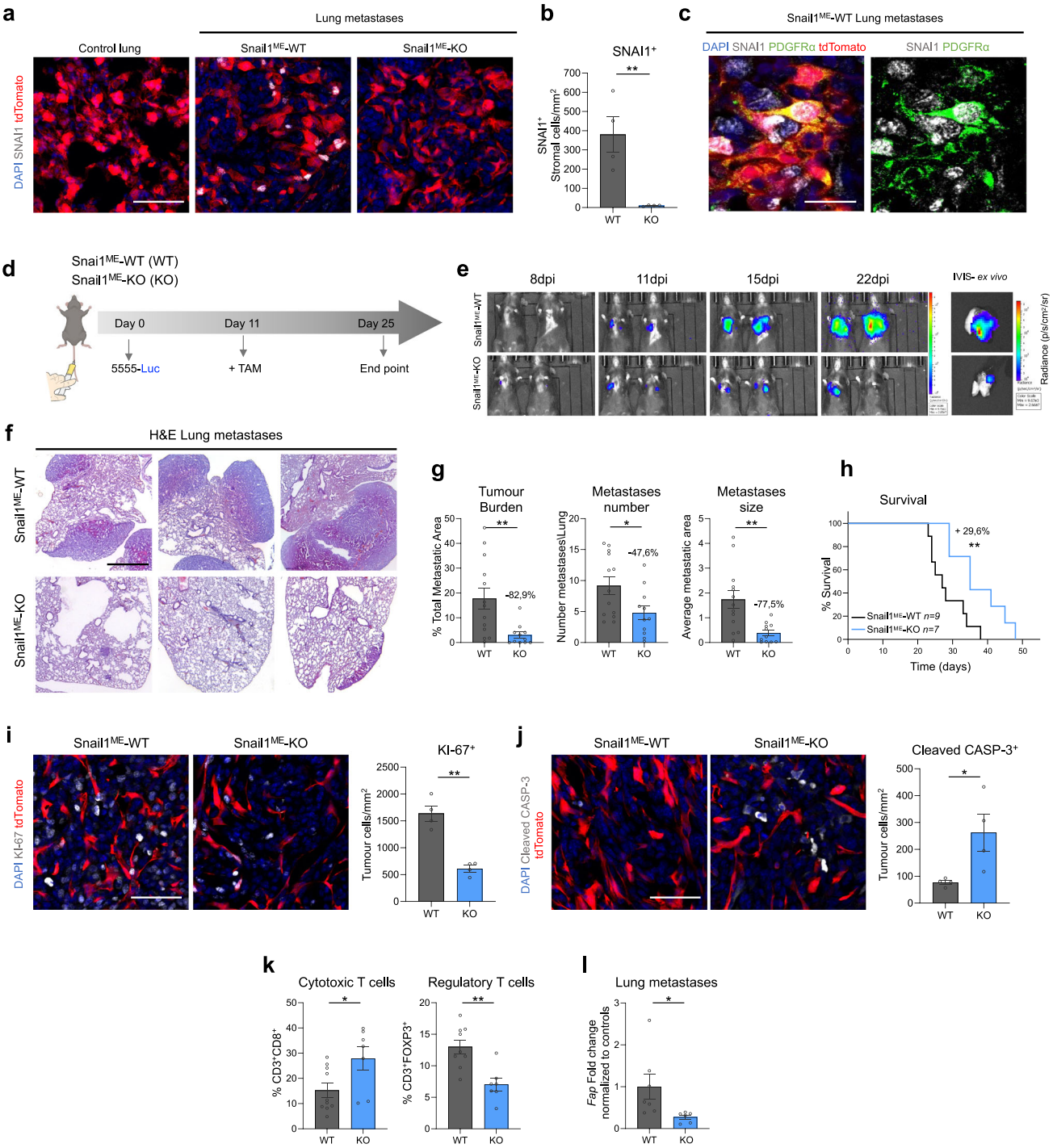

Fig. 5 Microenvironmental Snail1 depletion reduces melanoma metastatic burden and improves mice survival. a Representative images of immunolabelling for SNAI1 in control lung tissue and Braf^{V600E}-5555 lung metastases from Snail1^{ME}-WT and Snail1^{ME}-KO mice. Scale bar: 50 µm. **b** SNAI1 quantification after TAM administration in lung metastases from (**a**). **c** Representative images of double immunolabelling of SNAI1 (white) and PDGFRα (green) in Braf^{V600E}-5555 lung metastases from Snail1^{ME}-WT. Scale bar: 25 µm. **d** Experimental set-up of the in vivo strategy design to study the contribution of Snail1 to lung metastases progression in Snail1^{ME}-WT (WT) and Snail1^{ME}-KO (KO) mice. Created with BioRender.com. **e** Bioluminescent signal in mice from (**d**). The BLI scale is represented next to each panel. Units: p/s/cm2/sr ($n = 13$ WT and $n = 11$ KO). **f** Representative H&E-stained lung sections 25 days post-injection. Scale bar: 2 mm. **g** Tumour burden, number of metastases and metastases size, quantified in lungs from (**d**) ($n = 13$ WT and $n = 11$ KO). **h** Overall survival of Snail1^{ME}-WT and Snail1^{ME}-KO mice with melanoma lung metastases after Snail1-silencing compared to controls ($n = 9$ WT and $n = 7$ KO). **i** Representative images of immunolabelling for KI-67 and quantification ($n = 4$ per condition) in melanoma lung metastases from (**d**). Scale bar: 50 µm. **j** Representative images of immunolabelling for Cleaved-CASP3 and quantification ($n = 4$ per condition) in lung metastases from (**d**). Scale bar: 50 µm. **k** Graphs showing percentages of Cytotoxic T cells (CD3$^+$CD8a$^+$) and Regulatory T cells (CD3$^+$FOXP3$^+$) in lungs from (**d**) ($n = 10$ WT and $n = 7$ KO) assessed by flow cytometry. **l** *Fap* mRNA levels assessed by RT-qPCR in Snail1^{ME}-WT (WT) and Snail1^{ME}-KO (KO) lung metastases. Data are represented by Mean ± SEM and statistically significant differences are tested by unpaired two-tailed Student *t*-test. Each dot represents one animal (*=$p < 0.05$ and **=$p < 0.01$).

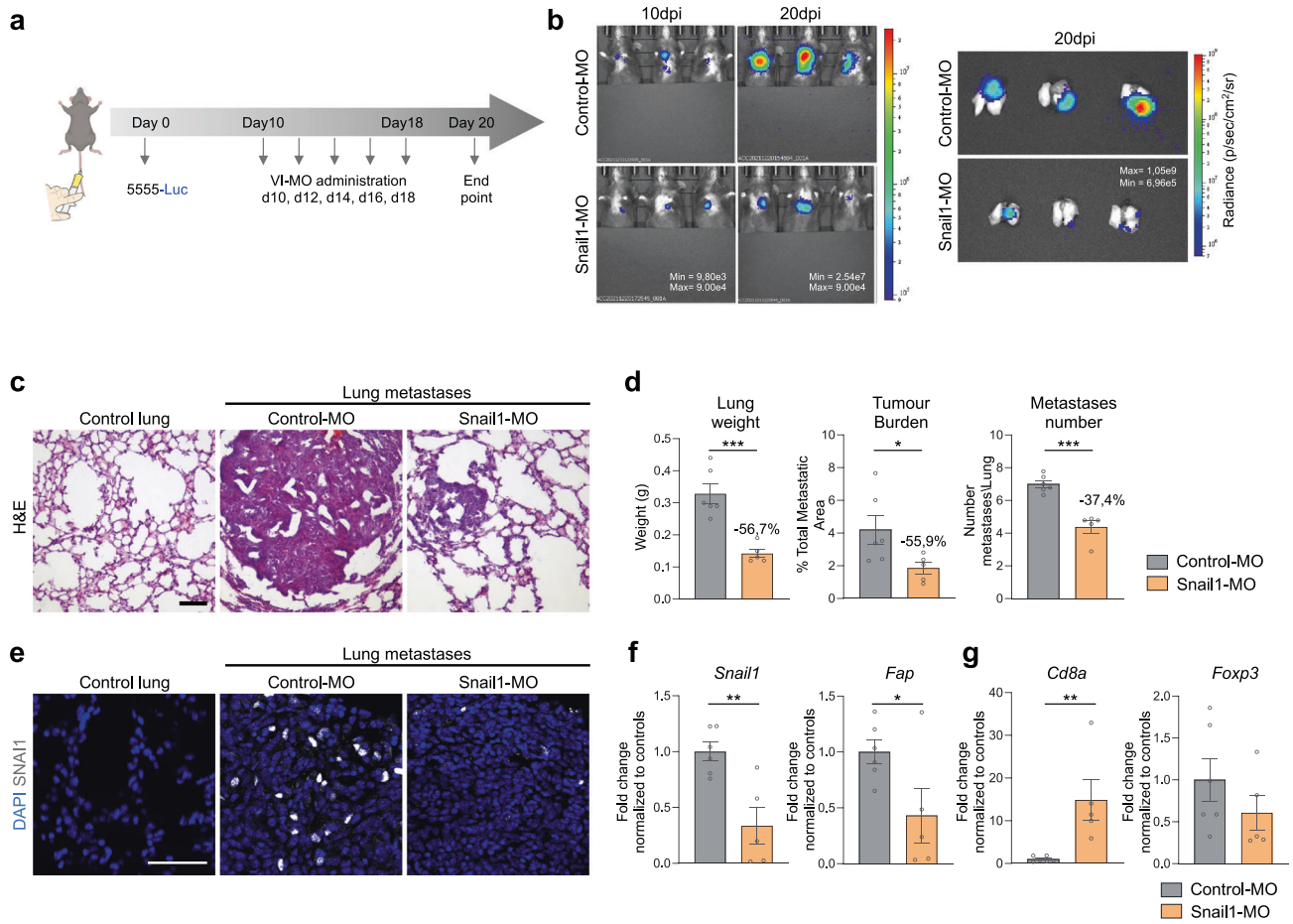

Fig. 6 Snail1 systemic targeting significantly reduces melanoma lung metastases in mice. a Scheme of the experimental approach. Nine days after tail vein injection of $Braf^{V600E}$-5555 cells, C57BL/6 mice were injected with vivo-morpholino (VI-MO) control (Control-MO) or Snail1 morpholino (Snail1-MO) every other day. Created with BioRender.com. **b** Bioluminescent signal in mice and lungs from (**a**). The BLI scale is represented in each panel. Units: p/s/cm2/sr. **c** Representative H&E-stained lung sections after VI-MO treatment. Scale: 100 µm. **d** Final lung weight, tumour burden and number of metastases from mice in (**a**) were quantified at the end of the experiment. **e** Representative images of immunolabelling for SNAI1 in lung sections after VI-MOs treatment. Scale bar: 50 µm. **f, g** *Snail1, Fap, Cd8a* and *Foxp3* mRNA expression assessed by RT-qPCR lung metastases from mice treated with Snail1-MO ($n = 6$ Control-MO and $n = 5$ Snail1-MO). Data are normalised to samples treated with Control-MO. Data are represented by Mean ± SEM and statistically significant differences are tested by unpaired two-tailed Student *t*-test. Each dot represents one animal (ns = not significant, * = $p < 0.05$, ** = $p < 0.01$, ***$p < 0.001$).

Tissue processing for flow cytometry

Tumours and lungs were mechanically dissociated using a scalpel blade followed by a cold and slow enzymatic digestion (2.5 mg/ml Collagenase A and 0.2 mg/ml DNAse I) (all from Roche) in PBS at 4 °C for 1 h using constant gentle orbital agitation. After the incubation, the cell suspension was filtered through a 40 µm cell strainer using a 2 ml syringe plunger. The content was centrifuged (5 min 350 g and 1 min 10.000 rpm) and pellets were resuspended in 1 ml of RBC lysis buffer for 4 min at RT. Subsequently, cells were centrifuged and resuspended in fluorescence-activated cell sorting (FACS) buffer.

FACS and flow cytometry

Prior to antibody staining, samples were blocked with Fc-block CD16/CD32 (Biolegend, 101320, 1:50) in FACS buffer for 10 min on ice to block nonspecific binding. For cell surface staining, cells were resuspended in the appropriate antibody cocktail and incubated for 30 min on ice protected from light. Samples were centrifuged and washed with a FACS buffer. For intracellular staining, cells were then collected and centrifuged for 5 min 350 g. Cells were fixed, permeabilized and stained for transcription factors using the True-Nuclear Transcription Factor Buffer Set (Biolegend, Cat# 424401) according to the manufacturer's instructions. Viability was assessed by staining with DAPI. Information and dilution for antibodies used for flow cytometry are listed in Supplementary Table 1. For fibroblast sorting cells, $PDGFR\alpha^{+}$ GFP^{-} $tdTomato^{+}$ were selected and sorted directly into a lysis solution from Arcturus PicoPure RNA Isolation Kit (Thermofisher). For sample validation, cells were plated in poly-L-lysine treated (Sigma) glass coverslips in 12-well plates and cultured for 24 h prior to IF. Immune cell profiling by flow cytometry was carried out by analysing 50.000 live singlets in each sample. All fluorescent data were analysed using BD FACSDiva Software (BD Bioscience).

Total RNA extraction cDNA synthesis and qPCR analysis

RNA extraction from FACS-isolated samples was performed following the instructions in the Arcturus PicoPure RNA Isolation Kit (Thermo Fisher). The RNA was collected in 15 µl of elution buffer (TE) and 1 µl was used for quantification and quality control using the Bioanalyzer High Sensitivity RNA chip. RNA extraction from bulk tumour or metastases samples was performed using the Illustra RNAspin Mini isolation kit (GE healthcare), following manufacturer's instructions. For cDNA synthesis, Maxima First Strand cDNA Synthesis kit (Thermo Fisher) was used, following the manufacturer's instructions. RT-qPCR was done using the Fast SYBR Green Mastermix (Applied Biosystems) and the primers listed in Supplementary Table 2. Relative levels of expression were calculated using a housekeeping gene and then experimental samples were normalised to their respective control.

RNA sequencing

RNA degradation and purity were assessed using the RNA Nano 6000 Assay for the Bioanalyzer 2100 (Agilent). Samples were sent to Novogene

Co. Sequencing libraries were generated using NEBNext® Single Cell/Low Input RNA Library Prep Kit for Illumina (NEB) following the manufacturer's recommendations. Sequencing was performed using a cBot Cluster Generation Sequencing using PE Cluster Kit cBot-HS (Illumina) according to the manufacturer's recommendation. After cluster generation, the library preparations were sequenced on an Illumina platform and 250 bp paired-end reads were generated.

RNA sequencing analysis

Raw data (raw reads) of FASTQ format were mapped to a mouse reference transcriptome (Mus_musculus.GRCm38.cdna.all.fa) built with Kallisto v.0.46.1. Read quantification to reference transcriptome was performed with Kallisto as well. The following steps were performed using R and RStudio. Tximport was used to import abundance.tsv files to R environment. EdgeR was used for differential expression analysis to obtain DEGlist objects and normalisation. The MatrixStats package was used to determine the statistics on the data. Data was filtered by choosing transcripts with at least 10 reads and later, at least one CPM in at least three samples. Normalisation factor TMM (trimmed mean of M-values) was applied. Limma and edgeR were used to obtain a final DEG list adjusted by BH (Benjamini-Hochberg) and sorted by p value < 0.05 and LFC > 1. The graphical constructs of the RNAseq data were performed using gplots, plotly, gprofiler2, clusterprofiler, GSEABase and GSEA software v4.3.2 [35, 62].

Transfection of plasmids and interfering RNAs

For RNA interference in NIH3T3 cells, siRNA obtained from Silencer® predesigned (Ambion) was used for Snail1 (Snail1 siRNA (antisense): AUAUUUGCAGUUGAAGAUCtt). Snai1-Myc plasmid was transfected in NIH3T3 cells seeded in six-well plates and 48 h after transfection cells were lysed for RNA extraction.

CYD19 drug administration

NIH3T3 cells were initially treated with TGFβ (2 ng/ml) for 24 h. Subsequently, the cells were exposed to either the vehicle or 5 nM of CYD19 (Cat#AOB11460, Aobious) in the presence of TGFβ for an additional 48 h. Following the treatment, NIH3T3 cells were subjected to IF or gene expression analysis.

Chromatin immunoprecipitation (ChIP) assay

NIH3T3 cells transfected with SNAI1-Myc were fixed at 80% confluency from 10 cm culture dish by adding 1% PFA for 10 min and subsequently quenched with glycine solution 0.125 M for 5 min. Then, the cells were harvested and pooled together from four plates, and the chromatin was isolated using the Pierce™ Magnetic ChIP Kit (Thermo Fisher) following the manufacturer's instructions. The sonication was performed in 15 cycles of 30-s on/off intervals in a Bioruptor® Pico sonication device (Diagenode). Finally, the immunoprecipitation and DNA isolation were performed using the same Pierce™ Magnetic ChIP Kit and the anti-Myc antibody listed in Supplementary Table 1. The isolated DNA was used for direct qPCR reaction.

Vivo-morpholino treatment

Snail1 Vivo-morpholino (Snail1-MO) (5′-TGAACTCTGCGGGAAGAGAAGA-GAC-3′) against the boundary sequences of the intron 1 and exon 2 of Snail1 gene and standard control morpholino (Control-MO) that targets human β-globin intron mutation (5′-CCTCTTACCTCATTACAATTTATA-3′) were designed (by Gene Tools). C57BL/6 mice aged 7 weeks were injected in the tail vein with $Braf^{V600E}$-5555 -Luciferase cells. 10 dpi, a solution containing Snail1-MO or Control-MO in saline (100 µl; 6 mg MO per kg) was injected in the tail vein of the corresponding mice every other day. After 20 days mice were sacrificed and lungs were processed, sectioned, and subjected to analysis.

Statistical analysis

All statistical tests were performed using GraphPad Prism 8 software. Student's t-test or One-way ANOVA with Bonferroni's multiple comparison test were performed to determine the significant values of the data. Kaplan-Meier data were analysed with the comparison of survival curves using the Long-rank (Mantel-Cox) test. All the values were shown as Mean values ± SEM (Standard Error of the Mean). Significant difference between groups were represented as follows: * = $p \le 0.05$, ** = $p \le 0.01$, *** = $p \le 0.001$ and **** = $p \le 0.0001$.

DATA AVAILABILITY

Single Cell RNAseq data from [42] are accessible via supplementary information or ArrayExpress: E-MTAB-7427. Bulk RNAseq data of sorted fibroblasts from [43] were accessed via EGAS00001002508. The datasets generated during the current study are available from the corresponding author on reasonable request.

REFERENCES

1. Davis LE, Shalin SC, Tackett AJ. Current state of melanoma diagnosis and treatment. Cancer Biol Ther. 2019;20:1366–79. https://doi.org/10.1080/15384047.2019.1640032.
2. Postovit LM, Seftor EA, Seftor REB, Hendrix MJC. Influence of the microenvironment on melanoma cell fate determination and phenotype. Cancer Res. 2006;66:7833–6.
3. Nieto MA, Huang RYYJ, Jackson RAA, Thiery JPP. Emt: 2016. Cell. 2016;166:21–45.
4. Nieto MA. Epithelial plasticity: a common theme in embryonic and cancer cells. Science. 2013;342:1234850.
5. Lu W, Kang Y. Epithelial-mesenchymal plasticity in cancer progression and metastasis. Dev Cell. 2019;49:361–74.
6. Hanahan D. Hallmarks of cancer: new dimensions. Cancer Discov. 2022;12:31–46.
7. Nieto MA. Context-specific roles of EMT programmes in cancer cell dissemination. Nat Cell Biol . 2017;19:416–8. https://doi.org/10.1038/ncb3520.
8. Dongre A, Rashidian M, Reinhardt F, Bagnato A, Keckesova Z, Ploegh HL. et al. Epithelial-to-mesenchymal transition contributes to immunosuppression in breast carcinomas. Cancer Res. 2017;77:3982–9.
9. Dongre A, Weinberg RA. New insights into the mechanisms of epithelial–mesenchymal transition and implications for cancer. Nat Rev Mol Cell Biol. 2019;20:69–84. https://doi.org/10.1038/s41580-018-0080-4.
10. Stanisavljevic J, Loubat-Casanovas J, Herrera M, Luque T, Peña R, Lluch A, et al. Snail1-expressing fibroblasts in the tumor microenvironment display mechanical properties that support metastasis. Cancer Res. 2015;75:284–95.
11. Alba-Castellón L, Olivera-Salguero R, Mestre-Farrera A, Peña R, Herrera M, Bonilla F, et al. Snail1-dependent activation of cancer-associated fibroblast controls epithelial tumor cell invasion and metastasis. Cancer Res. 2016;76:6205–17.
12. Cortés M, Sanchez-Moral L, de Barrios O, Fernández-Aceñero MJ, Martínez-Campanario M, Esteve-Codina A, et al. Tumor-associated macrophages (TAMs) depend on ZEB1 for their cancer-promoting roles. EMBO J. 2017;36:3336–55.
13. Blanco-Gomez A, Hontecillas-Prieto L, Corchado-Cobos R, García-Sancha N, Salvador N, Castellanos-Martín A, et al. Stromal SNAI2 is required for ERBB2 breast cancer progression. Cancer Res. 2020;80:5216–30.
14. Lee K-W, Yeo S-Y, Gong J-R, Koo O-J, Sohn I, Lee WY, et al. PRRX1 is a master transcription factor of stromal fibroblasts for myofibroblastic lineage progression. Nat Commun. 2022;13:1–23.
15. Sahai E, Astsaturov I, Cukierman E, DeNardo DG, Egeblad M, Evans RM, et al. A framework for advancing our understanding of cancer-associated fibroblasts. Nat Rev Cancer. 2020;20:174–86. https://doi.org/10.1038/s41568-019-0238-1.
16. Lavie D, Ben-Shmuel A, Erez N, Scherz-Shouval R. Cancer-associated fibroblasts in the single-cell era. Nat Cancer. 2022;3:793–807.
17. Vandamme N, Denecker G, Bruneel K, Blancke G, Akay O, Taminau J, et al. The EMT transcription factor ZEB2 promotes proliferation of primary and metastatic melanoma while suppressing an invasive, mesenchymal-like phenotype. Cancer Res. 2020;80:2983–95.
18. Caramel J, Papadogeorgakis E, Hill L, Browne GJ, Richard G, Wierinckx A, et al. A Switch in the expression of embryonic EMT-inducers drives the development of malignant melanoma. Cancer Cell. 2013;24:466–80.
19. Denecker G, Vandamme N, Akay Ö, Koludrovic D, Taminau J, Lemeire K, et al. Identification of a ZEB2-MITF-ZEB1 transcriptional network that controls melanogenesis and melanoma progression. Cell Death Differ. 2014;21:1250–61.
20. Vandamme N, Berx G. Melanoma cells revive an embryonic transcriptional network to dictate phenotypic heterogeneity. Front Oncol. 2014;4:1–6.
21. Karras P, Bordeu I, Pozniak J, Nowosad A, Pazzi C, Raemdonck N, et al. A cellular hierarchy in melanoma uncouples growth and metastasis. Nature. 2022;610:190–8.
22. Kudo-Saito C, Shirako H, Takeuchi T, Kawakami Y. Cancer metastasis is accelerated through immunosuppression during snail-induced EMT of cancer cells. Cancer Cell. 2009;15:195–206. http://ac.els-cdn.com/S1535610809000324/1-s2.0-S1535610809000324-main.pdf?_tid=ee389d7c-c684-11e5-bb54-00000aacb361&acdnat=1454071174_e8bca0dd8025cf245a3948d1a9866a01.
23. Brenot A, Knolhoff BL, Denardo DG, Longmore GD. SNAIL1 action in tumor cells influences macrophage polarization and metastasis in breast cancer through altered GM-CSF secretion. Oncogenesis. 2018;7:32. https://doi.org/10.1038/s41389-018-0042-x.
24. Cheng H-Y, Hsieh C-H, Lin P-H, Chen Y-T, Hsu DS, Tai S-K. et al. Snail- regulated exosomal microRNA- 21 suppresses NLRP3 inflammasome activity to enhance cisplatin resistance. J Immunother Cancer. 2022;10:1–16.

25. Cano A, Pérez-Moreno MA, Rodrigo I, Locascio A, Blanco MJ, Del Barrio MG, et al. The transcription factor Snail controls epithelial-mesenchymal transitions by repressing E-cadherin expression. Nat Cell Biol. 2000;2:76–83.
26. Dankort D, Curley DP, Cartlidge RA, Nelson B, Karnezis AN, Damsky WE, et al. BrafV600E cooperates with Pten loss to induce metastatic melanoma. Nat Genet. 2009;41:544–52.
27. Dhomen N, Reis-filho JS, Dias R, Hayward R, Savage K, Delmas V, et al. Oncogenic braf induces melanocyte senescence and melanoma in mice. Cancer Cell. 2009;15:294–303. https://doi.org/10.1016/j.ccr.2009.02.022.
28. Hirata E, Girotti MR, Viros A, Hooper S, Spencer-Dene B, Matsuda M, et al. Intravital imaging reveals how BRAF inhibition generates drug-tolerant microenvironments with high integrin β1/FAK signaling. Cancer Cell. 2015;27:574–88. https://doi.org/10.1016/j.ccell.2015.03.008.
29. Ruzankina Y, Pinzon-Guzman C, Asare A, Ong T, Pontano L, Cotsarelis G, et al. Deletion of the developmentally essential gene ATR in adult mice leads to age-related phenotypes and stem cell loss. Cell Stem Cell. 2007;1:113–26.
30. Rowe RG, Li X, Hu Y, Saunders TL, Virtanen I, Garcia de Herreros A, et al. Mesenchymal cells reactivate Snail1 expression to drive three-dimensional invasion programs. J Cell Biol. 2009;184:399–408.
31. Jung S, Aliberti J, Graemmel P, Sunshine MJ, Kreutzberg GW, Sher A, et al. Analysis of fractalkine receptor CX 3 CR1 function by targeted deletion and green fluorescent protein reporter gene insertion. Mol Cell Biol. 2000;20:4106–14.
32. Geissmann F, Jung S, Littman DR. Blood monocytes consist of two principal subsets with distinct migratory properties. Immunity. 2003;19:71–82.
33. Nieto MA, Bennett MF, Sargent MG, Wilkinson DG. Cloning and developmental expression of Sna, a murine homologue of the drosophila snail gene. Development. 1992;116:227–37.
34. Carver EA, Jiang R, Lan Y, Oram KF, Gridley T. The mouse snail gene encodes a key regulator of the epithelial-mesenchymal transition. Mol Cell Biol. 2001;21:8184–8.
35. Subramanian A, Tamayo P, Mootha VK, Mukherjee S, Ebert BL, Gillette MA, et al. Gene set enrichment analysis: a knowledge-based approach for interpreting genome-wide expression profiles. Proc Natl Acad Sci USA. 2005;102:15545–50.
36. Wiedemann GM, Knott MML, Vetter VK, Rapp M, Haubner S, Fesseler J, et al. Cancer cell-derived IL-1α induces CCL22 and the recruitment of regulatory T cells. Oncoimmunology. 2016;5:e1175794. https://doi.org/10.1080/2162402X.2016.1175794.
37. Ren J, Lan T, Liu T, Liu Y, Shao B, Men K. et al. CXCL13 as a novel immune checkpoint for regulatory B cells and its role in tumor metastasis. J Immunol. 2022;208:2425–35.
38. Weber R, Riester Z, Hüser L, Sticht C, Siebenmorgen A, Groth C, et al. IL-6 regulates CCR5 expression and immunosuppressive capacity of MDSC in murine melanoma. J Immunother Cancer. 2020;8:1–13.
39. Kuehnemuth B, Piseddu I, Wiedemann GM, Lauseker M, Kuhn C, Hofmann S, et al. CCL1 is a major regulatory T cell attracting factor in human breast cancer. BMC Cancer. 2018;18:1–6.
40. Martinenaite E, Munir Ahmad S, Hansen M, Met Ö, Westergaard MW, Larsen SK, et al. CCL22-specific T Cells: Modulating the immunosuppressive tumor microenvironment. Oncoimmunology. 2016;5:e1238541.
41. Erez N, Truitt M, Olson P, Hanahan D. Cancer-associated fibroblasts are activated in incipient neoplasia to orchestrate tumor-promoting inflammation in an NF-κB-dependent manner. Cancer Cell. 2010;17:135–47. https://doi.org/10.1016/j.ccr.2009.12.041.
42. Davidson S, Efremova M, Riedel A, Mahata B, Pramanik J, Huuhtanen J, et al. Single-Cell RNA sequencing reveals a dynamic stromal niche that supports tumor growth. Cell Rep. 2020;31:107628 https://doi.org/10.1016/j.celrep.2020.107628.
43. Costa A, Kieffer Y, Scholer-Dahirel A, Pelon F, Bourachot B, Cardon M, et al. Fibroblast heterogeneity and immunosuppressive environment in human breast cancer. Cancer Cell. 2018;33:463–479.e10.
44. Jenkins RW, Barbie DA, Flaherty KT. Mechanisms of resistance to immune checkpoint inhibitors. Br J Cancer. 2018;118:9–16. https://doi.org/10.1038/bjc.2017.434.
45. Kovács SA, Győrffy B. Transcriptomic datasets of cancer patients treated with immune-checkpoint inhibitors: a systematic review. J Transl Med. 2022;20:1–15. https://doi.org/10.1186/s12967-022-03409-4.
46. Lánczky A, Győrffy B. Web-based survival analysis tool tailored for medical research (KMplot): development and implementation. J Med Internet Res. 2021;23:1–7.
47. Yang X, Lin Y, Shi Y, Li B, Liu W, Yin W, et al. FAP Promotes immunosuppression by cancer-associated fibroblasts in the tumor microenvironment via STAT3-CCL2 Signaling. Cancer Res. 2016;76:4124–35.
48. Takahashi H, Sakakura K, Kawabata-Iwakawa R, Rokudai S, Toyoda M, Nishiyama M, et al. Immunosuppressive activity of cancer-associated fibroblasts in head and neck squamous cell carcinoma. Cancer Immunol Immunother. 2015;64:1407–17.
49. Cremasco V, Astarita JL, Grauel AL, Keerthivasan S, MacIsaac K, Woodruff MC, et al. FAP delineates heterogeneous and functionally divergent stromal cells in immune-excluded breast tumors. Cancer Immunol Res. 2018;6:1472–85.
50. Zhang Y, Ertl HCJ. Depletion of FAP+ cells reduces immunosuppressive cells and improves metabolism and functions CD8.T cells within tumors. Oncotarget. 2016;7:23282–99.
51. Cohen N, Shani O, Raz Y, Sharon Y, Hoffman D, Abramovitz L, et al. Fibroblasts drive an immunosuppressive and growth-promoting microenvironment in breast cancer via secretion of Chitinase 3-like 1. Oncogene. 2017;36:4457–68. https://doi.org/10.1038/onc.2017.65.
52. Li HM, Bi YR, Li Y, Fu R, Lv WC, Jiang N, et al. A potent CBP/p300-Snail interaction inhibitor suppresses tumor growth and metastasis in wild-type p53-expressing cancer. Sci Adv. 2020;6:eaaw8500.
53. Villarejo A, Cortés-Cabrera Á, Molina-Ortíz P, Portillo F, Cano A. Differential role of snail1 and snail2 zinc fingers in E-cadherin repression and epithelial to mesenchymal transition. J Biol Chem. 2014;289:930–41.
54. Grande MT, Sánchez-Laorden B, López-Blau C, De Frutos CA, Boutet A, Arévalo M, et al. Snail1-induced partial epithelial-to-mesenchymal transition drives renal fibrosis in mice and can be targeted to reverse established disease. Nat Med. 2015;21:989–97.
55. Chen J, Hu S, Wang H, Zhao T, Song Y, Zhong X, et al. Integrated analysis reveals the pivotal interactions between immune cells in the melanoma tumor microenvironment. Sci Rep. 2022;12:1–16. https://doi.org/10.1038/s41598-022-14319-2.
56. Boutet A, De Frutos CA, Maxwell PH, Mayol MJ, Romero J, Nieto MA. Snail activation disrupts tissue homeostasis and induces fibrosis in the adult kidney. EMBO J. 2006;25:5603–13.
57. Luo H, Xia X, Huang L-B, An H, Cao M, Kim GD. et al. Pan-cancer single-cell analysis reveals the heterogeneity and plasticity of cancer- associated fibroblasts in the tumor microenvironment. Nat Commun. 2022;13:6619.
58. Hsu DSS, Wang HJ, Tai SK, Chou CH, Hsieh CH, Chiu PH, et al. Acetylation of snail modulates the cytokinome of cancer cells to enhance the recruitment of macrophages. Cancer Cell. 2014;26:534–48. https://doi.org/10.1016/j.ccell.2014.09.002.
59. Rembold M, Ciglar L, Omar Yáñez-Cuna J, Zinzen RP, Girardot C, Jain A, et al. A conserved role for Snail as a potentiator of active transcription. Genes Dev. 2014;28:167–81.
60. Carlino MS, Larkin J, Long GV. Immune checkpoint inhibitors in melanoma. Lancet. 2021;398:1002–14. https://doi.org/10.1016/S0140-6736(21)01206-X.
61. Rivers LE, Young KM, Rizzi M, Jamen F, Psachoulia K, Wade A, et al. PDGFRA/NG2 glia generate myelinating oligodendrocytes and piriform projection neurons in adult mice. Nat Neurosci. 2008;11:1392–401.
62. Mootha VK, Lindgren CM, Eriksson KF, Subramanian A, Sihag S, Lehar J, et al. PGC-1α-responsive genes involved in oxidative phosphorylation are coordinately downregulated in human diabetes. Nat Genet. 2003;34:267–73.

ACKNOWLEDGEMENTS

We thank members of Berta Sanchez-Laorden and Angela Nieto's labs for helpful discussions and comments along the project. We thank Joan Galceran and Khalil Kass Youssef for advice and help with the ChIP experiments and Jose Vicente Sanchez-Mut for advice with the data analysis. We also thank Isabel Perez Otaño for the PDGFRα-CreERT2 mice and the Imaging (Verona Villar and Giovanna Exposito) and OMICS (Antonio Caler) facilities for the technical support. This work was supported by grants SAF2016-75702-R and PID2019-106852-RBI00 (to BS-L), RTI2018-096501-B-I00 and PID2021-125682NB-I00 (to MAN) funded by MCIN/AEI/ 10.13039/501100011033 and ERDF, the Melanoma Research Alliance (https://doi.org/10.48050/pc.gr.91574 to B.S-L), the FERO Foundation (to B.S-L) and the AECC Scientific Foundation (FC_AECC PROYE19073NIE to MAN). MA-P and FC-T were recipients of a FPI predoctoral contract. FJR-B and FG hold contracts from the Generalitat Valenciana (APOSTD and ACIF, respectively). We also acknowledge financial support from the Spanish State Research Agency, through the 'Severo Ochoa Programme' for Centres of Excellence in R&D (SEV-2017-0273) and the Generalitat Valenciana through the 'Prometeo Programme' for Groups of Excellence (CIPROM/2021/045).

AUTHOR CONTRIBUTIONS

MA-P performed most experiments, analysed, and interpreted the data, and contributed to writing the manuscript. FJR-B analysed and interpreted the transcriptomic data and performed some experiments, FC-T, FG and CL-B performed experiments. MAN provided the UBC-Cre-Snail1^{loxp} mice and helped in the interpretation of data. BS-L conceived the project, interpreted the data, and wrote the manuscript.

COMPETING INTERESTS

The authors declare no competing interests.

ADDITIONAL INFORMATION

Supplementary information The online version contains supplementary material available at https://doi.org/10.1038/s41388-023-02793-5.

Correspondence and requests for materials should be addressed to Berta Sanchez-Laorden.

Reprints and permission information is available at http://www.nature.com/reprints

Publisher's note Springer Nature remains neutral with regard to jurisdictional claims in published maps and institutional affiliations.